www.acsnano.org

# Stress and Curvature Effects in Layered 2D Ferroelectric CuInP<sub>2</sub>S<sub>6</sub>

Yongtao Liu,\* Anna N. Morozovska, Ayana Ghosh, Kyle P. Kelley, Eugene A. Eliseev, Jinyuan Yao, Ying Liu, and Sergei Kalinin\*



Downloaded via PENNSYLVANIA STATE UNIV on March 25, 2024 at 14:27:38 (UTC). See https://pubs.acs.org/sharingguidelines for options on how to legitimately share published articles.

Cite This: ACS Nano 2023, 17, 22004-22014



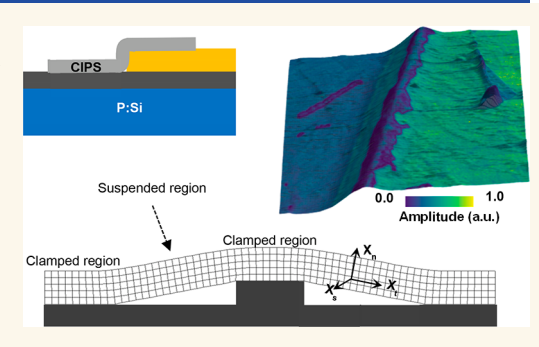
**ACCESS** I

III Metrics & More

Article Recommendations

Supporting Information

ABSTRACT: Nanoscale ferroelectric 2D materials offer the opportunity to investigate curvature and strain effects on materials functionalities. Among these, CuInP<sub>2</sub>S<sub>6</sub> (CIPS) has attracted tremendous research interest in recent years due to combination of room temperature ferroelectricity, scalability to a few layers thickness, and ferrielectric properties due to coexistence of 2 polar sublattices. Here, we explore the local curvature and strain effect on polarization in CIPS via piezoresponse force microscopy and spectroscopy. To explain the observed behaviors and decouple the curvature and strain effects in 2D CIPS, we introduce the finite element Landau–Ginzburg–Devonshire model, revealing strong changes in hysteresis characteristics in regions subjected to tensile and compressive strain. The piezoresponse force



microscopy (PFM) results show that bending induces ferrielectric domains in CIPS, and the polarization-voltage hysteresis loops differ in bending and nonbending regions. These studies offer insights into the fabrication of curvature-engineered nanoelectronic devices.

**KEYWORDS:** CuInP<sub>2</sub>S<sub>6</sub>, ferroelectric, flexoelectric, strain, curvature, 2D materials, piezoresponse force microscopy

ithin two decades since the work by Geim and Novoselov in 2004, 2D materials including graphene and transition metal dichalcogenides have become one of the central topics of research in condensed matter physics, quantum materials, and electronics. In addition to the intrinsic excellent physical properties of 2D materials, e.g., high electron mobility and thermal conductivity, new phenomena have been discovered in the twisted bilayers as driven by emergent electronic instabilities. 5-8 Over the last several years interest shifted toward the layered materials that support additional functionalities including ferromagnetic9 and ferroelectric, 10 this opening the route to ferroelectricity at atomic thicknesses. Since 2D materials can withstand significantly large curvature and strain, these materials systems allow to get insight into novel phenomena based on the curvature<sup>11</sup> and strain effects. With the coupling between polarization and strain effect being significant even for 3D ferroelectrics, this is expected to be even more pronounced in 2D ferroelectric materials that can support larger curvatures. 14-18

Of these systems,  $\text{CuInP}_2S_6$  (CIPS) was discovered to exhibit ferroelectricity at room temperature,  $^{10,19-21}$  making it highly promising for advanced applications utilizing ferrielectricity and antiferrielectricity down to the limit of a single layer.  $^{19,22-24}$  Ferrielectricity, the equivalent of ferrimagnetism, can be termed as an antiferroelectric order, but with a

switchable spontaneous polarization created by two sublattices with spontaneous dipole moments that are antiparallel and different in magnitude.<sup>25</sup>

In the context of the 2D material, of particular interest is the control of polarization via stress and curvature. The curvature is expected to directly contribute to the flexoelectric field in the material and can also affect the ferroelectric phase stability. At the same time, stress is one of the well-recognized control parameters in ferroelectric thin films that can couple to polarization and induce transitions between structural variants. For Cu-based layered chalcogenides, stress-induced phase transitions  $^{26}$  and strain engineering  $^{14,16}$  become especially important in ultrathin films of  $\text{CuInP}_2(\text{S,Se})_6$ ,  $^{10,27,28}$  Despite the significant fundamental and practical interest in  $\text{bulk}^{29}$  and nanosized  $\text{CuInP}_2(\text{S,Se})_6$ ,  $^{30}$  the influence of stress and strains on the local switching of its spontaneous polarization is explored only weakly. From a theoretical perspective, there has been very little effort on both mesoscopic and atomistic levels

Received: September 9, 2023
Revised: October 16, 2023
Accepted: October 19, 2023
Published: November 2, 2023





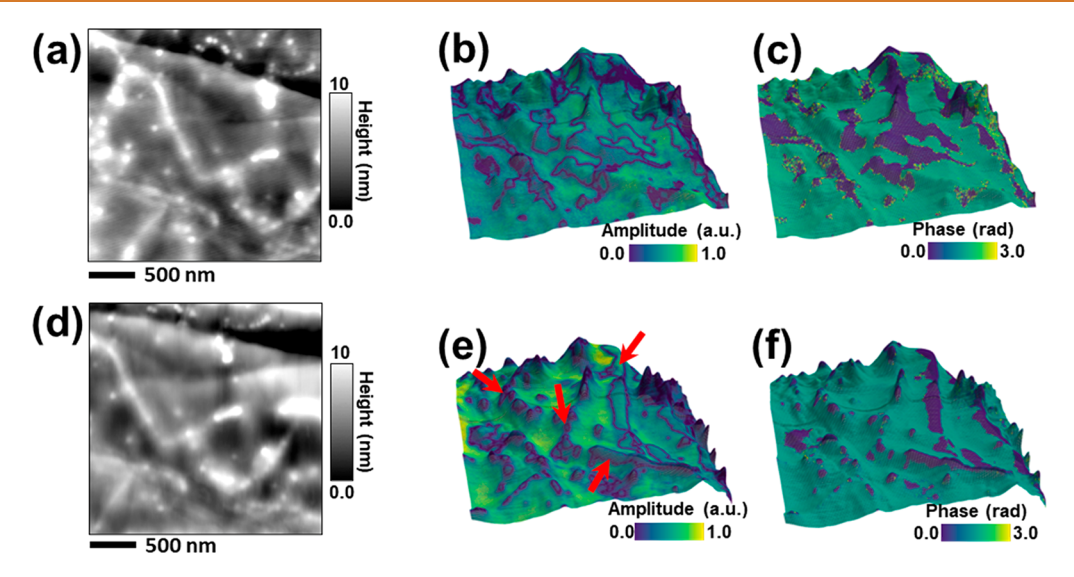


Figure 1. Band excitation piezoresponse force microscopy (BEPFM) shows the relationship between domain evolution and morphology in CIPS. (a) Topography of the original CIPS flake. (b,c) BEPFM results of the original CIPS flake. (d) Topography of the CIPS flake after stored in vacuum for 11 days. (e,f) BEPFM results of the CIPS flake after being stored in a vacuum for 11 days. The BEPFM results in (b,c) and (e,f) are plotted over topography to highlight the relationship between domains and morphology, where the color represents PFM amplitude or phase and the geometry represents topography. Obviously, after 11 days, the domain walls move toward the high curvature regions as indicated by red arrows in (e). The thickness of this CIPS flake is  $\sim$ 30 nm.

of theory. At the same time, from an experimental perspective, while curvature in 2D materials can be measured directly from observed topography, the strain state is determined by the nonobservable interactions such as adhesion to the substrate, friction at the film—substrate interface, and sample history.

Previously, mechanical modulation of polarization in a CIPS thin film was discovered. Chen et al. was able to artificially generate large-scale stripe domains of hundreds of microns by corrugating the CIPS flake, where it is believed that the giant strain gradient is introduced via high curvature. 16 Similar curvature induced domains were observed by several other groups. 14,18 Similarly, mechanical switching of polarization in CIPS has been demonstrated. 14,18 This effect was attributed to flexoelectricity owing to the formation of a giant strain gradient. Almost at the same time, another work revealed strong second harmonic generation (SHG), ~160-fold enhancement compared to unstrained region, of wrinkle nanostructures in CIPS, this SHG enhancement can be modulated by the applied strain.<sup>17</sup> Angle resolved SHG also revealed a distorted pattern which was attributed to a photoelastic effect.1

Here, we investigate the curvature and strain effects in the 2D CIPS nanoflakes using the combination of ambient scanning probe microscopy with the mesoscopic and finite element methods and Landau—Ginsburg—Devonshire (LGD) simulation. We show that bending induces domains in CIPS and the polarization-voltage hysteresis loops in bending regions differ from those in nonbending regions. The simulation provides insights into the mechanism behind these observations.

### **RESULTS AND DISCUSSION**

Single crystal CuInP<sub>2</sub>S<sub>6</sub> was synthesized through the chemical vapor transport (CVT) method.<sup>31</sup> The Cu, In, P, and S powders were mixed in a stoichiometric ratio and loaded into a quartz tube (10 mm inside diameter, 18 cm length). The transport agent, 16 mg I<sub>2</sub>, was added. The quartz tube was

sealed under vacuum and then heated up in a horizontal double-zone furnace with the hot and cold ends set at 750 and 650 °C, respectively. After 14 days, the furnace was shut down, the quartz tube was naturally cooled to room temperature, and yellow platelike crystals were found at the cold end of the quartz tube. To bend the CIPS flakes, 30 nm Pt and 5/45 nm Ti/Au bottom electrodes were patterned on  $SiO_2$  on a Si substrate by photolithography and created by electron-beam evaporation and lift-off process. CIPS flakes are mechanically exfoliated from the bulk crystal and transferred onto prepatterned bottom electrodes by the polydimethylsiloxane (PDMS) dry transfer technique. Then, the CIPS flakes at the edge of the bottom electrode are bent.

Figure 1 shows band excitation piezoresponse force microscopy (BEPFM) results of the typical ferroelectric domains of a 50 nm thick CIPS flake on Pt/SiO<sub>2</sub>/Si substrate, which are very similar to previous results. <sup>10,32,33</sup> In BEPFM and other PFM measurements in this work, the sample is grounded through Si with silver paint and the driving bias amplitude for PFM is 1 V. Shown in Figure 1a is the topography of the BEPFM measurement area. BEPFM amplitude and phase over the topography (where color represents amplitude and phase signals, and the geometry represents the topography signal) in Figure 1b,c, respectively, show the ferroelectric domain structure in the pristine CIPS flake. It is seen that the domain distribution is somehow correlated to the topography variation. After the CIPS flake was stored under vacuum conditions for 11 days, a variation of the ferroelectric domain is observed in the BEPFM results in Figure 1e,f. In comparison with the pristine domain structure in Figure 1b,c, it is obvious that the domain walls move toward the area with a larger topography variation, i.e., larger curvature area; examples are marked by red arrows in Figure 1e. This spontaneous domain wall motion induces a shrinkage of dark domains, as shown in Figure 1f; as such, the final domain walls mostly locate between concave and convex areas. Here note that no distinct topography is observed as a comparison of Figure 1a,d.

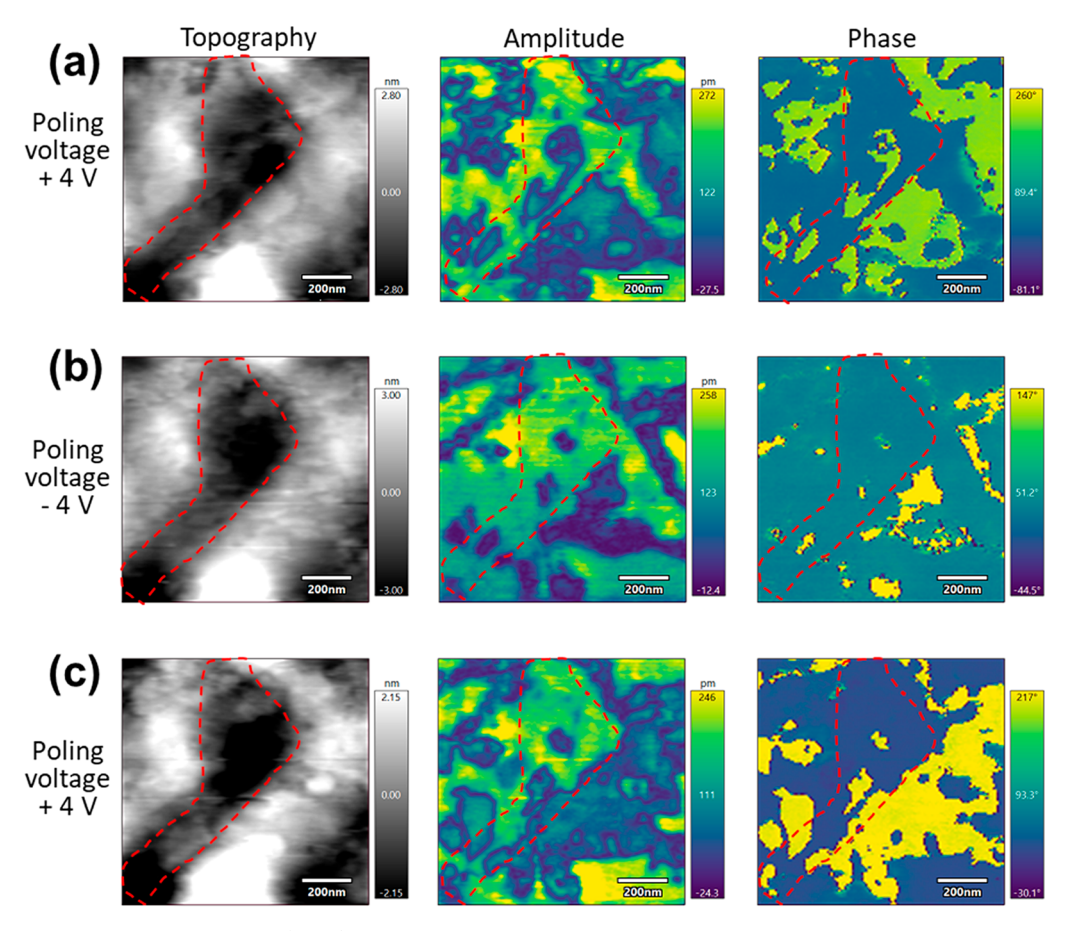


Figure 2. Piezoresponse force microscopy (PFM) shows the relationship between domain evolution and morphology in CIPS upon DC poling. (a) Topography and PFM results of the CIPS flake under +4 V poling. (b) Topography and PFM results of the CIPS flake under -4 V poling. (c) Topography and PFM results of the CIPS flake under +4 V poling. Major topography features are marked by red dashed lines in images. It is shown that the domain walls tend to locate near the high curvature regions. The thickness of this CIPS flake is ~30 nm.

The domain wall motion toward or formation near a high curvature area is also observed in the electric poling process, as shown in Figure 2. Figure 2a—c shows the topography with PFM amplitude and phase images after +4, -4, and +4 V poling, respectively. The high curvature regions observed from topography are marked with red dashed lines in all images. The results indicate domain walls tend to move or form near high curvature regions. Noteworthily, for vdW ferroelectrics, electric field writing often results in leakage current, and/or material breakdown, which does not guarantee effective polarization switch. <sup>19,34,35</sup> Nonetheless, in this work, a domain wall motion toward the high curvature area is observed.

The domain wall motion toward a high curvature area induced by mechanical and electric modulation motivated us to explore the correlation between curvature and ferroelectric domains in CIPS flakes. We intentionally introduced curvature in CIPS flakes by transferring the flakes on the edge of the bottom electrodes, thus, the CIPS flake at the edge forms a large curvature, as shown in Figure 3a. The atomic force microscopy (AFM) topography result in Figure 3b confirms the curvature formed near the edge area. Next, BEPFM imaging and spectroscopy measurements were performed to investigate the ferroelectricity near the large curvature area. Shown in Figure 3c—e and Figure 3f—h are the out-of-plane and in-plane BEPFM results, respectively. The results in Figure 3c,d show a domain along the down-bending edge, while no domain is seen in the up-bending edge. We ascribe this

behavior as that the down-bending reverses the polarization. In-plane BEPFM amplitude in Figure 3f shows a slightly higher amplitude response corresponding to the domain walls, which may suggest in-plane polarization at domain walls. Then, the corresponding resonance frequency map in Figure 3e indicates a frequency shift over the suspended region; this frequency shift is further confirmed by a blue-laser-driven contact resonance AFM measurement (in contrast to electric driven in PFM) shown in Figure 3i. The frequency shift is relatively small, usually a resonance frequency shift is associated with the local mechanical stiffness change. However, note that the frequency shift area does not correspond to the ferroelectric domain here, where the domains formed at the down-bending edge, but the frequency shift happens at the titled area (probably owing to tip—sample contact variation).

Band excitation piezoresponse spectroscopy (BEPS) measurements were further performed to explore the polarization dynamics in this area. In BEPS, a DC pulse ( $V_{\rm dc}$ ) is applied to switch the local polarization (see Figure 4a). Here we note that the electrically driven polarization switching in CIPS is challenging, <sup>36</sup> because the application of electric field often induces ion migration and sample damages. Nevertheless, we investigated the deformation induced by  $V_{\rm dc} + V_{\rm ac}$ ). We applied a triangular DC waveform with a magnitude of 8 V to the sample. Shown in Figure 4a are the bending-induced domain structures of the BEPS measurement area, and shown in Figure 4b are two examiners BEPS piezoresponse vs  $V_{\rm dc}$ 

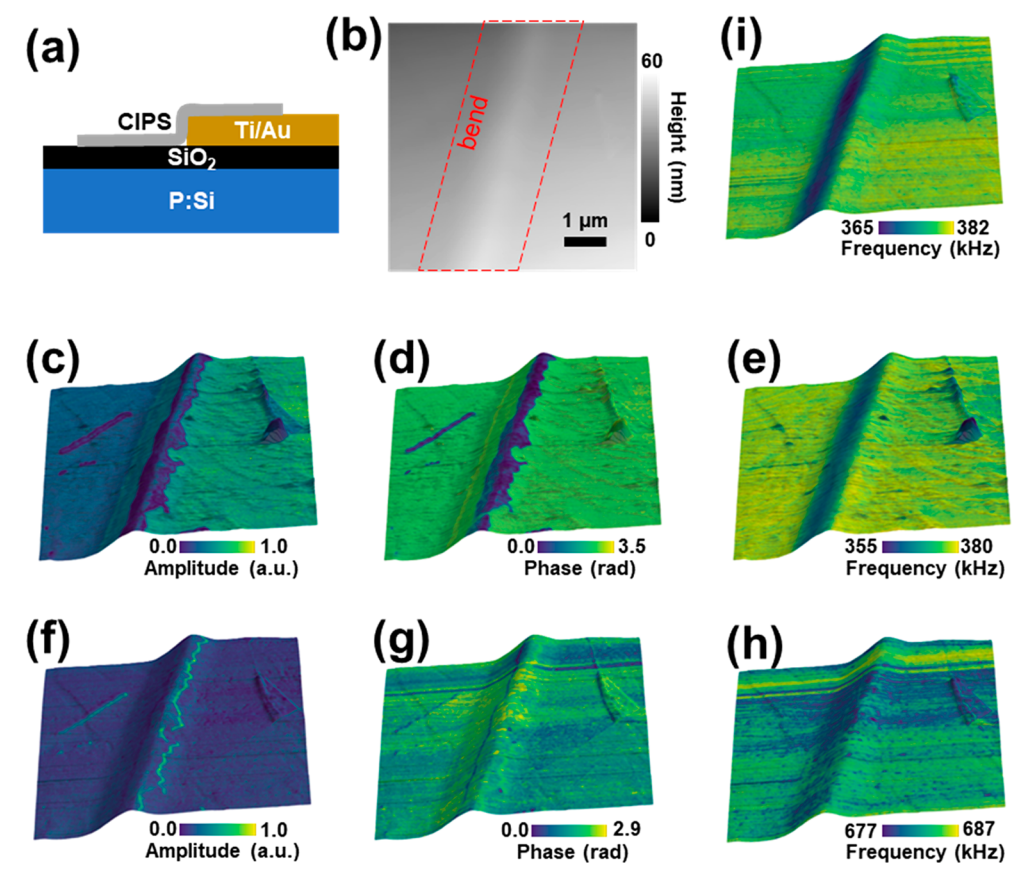


Figure 3. Artificial domains induced by bending. (a) Device structure for bending the CIPS flake. (b) AFM topography showing the bend structure. (c-e) Vertical BEPFM amplitude, phase, and frequency showing the domain structure induced by bending. (f-h) Lateral BEPFM amplitude, phase, and frequency showing the in-plane response of bending-induced domains. (i) Blue-laser-driven CR-AFM showing the mechanical property of bending-induced domains. The resonant frequency variation at the bend regions is lower by 20 kHz, indicating the material here is softer. The thickness of this CIPS flake is  $\sim 60$  nm.

loops, indicating the spatial variation of BEPS response in the measurement area. To better understand the BEPS response of the bending-induced domain, we created three masks (as shown in Figure 4c) to mask out the BEPS results corresponding to the high curvature area (green mask) and no-curvature areas (blue and red masks). The averaged BEPS loops corresponding to the masked areas are shown in Figure 4d. It is obvious that the BEPS loops of the high curvature area show a distinct shape compared to the no-curvature area. Noteworthily, the grounding here is achieved through the Si substrate, which may lead to nonuniform electric field through three regions. However, the major difference between the hysteresis loops from the curved region and the uncurved region is the loop shape, which is unlikely originated from the difference in applied electric field. Also, in CIPS the ionic response can originate from the transfer of Cu ions, 35 the case is not a consideration here because we focus on the polarization behavior.

The red and blue loops in Figure 4d, which are the so-called "minor loops", correspond to partial switching. Such curves appear when the amplitude of applied bias (8 V in the considered case) is too small to switch locally the spontaneous polarization. That is why both these minor loops have almost the same saturation value (about 6 au) and correspond to the situation far from the domain wall. The same "bias window" is enough to switch locally the polarization near the domain wall, and thus the green loop is open and symmetric. The

application of LGD approach for the description of the bias window dependence on the distance from domain walls has been studied by us earlier both experimentally and theoretically.<sup>37</sup> The bias window is maximal when the tip apex is placed far from the wall, minimal when the tip apex is near the wall, and zero (in the static limit) if the tip is placed exactly at the wall plane (see Figure C1). Moreover, the apparent switching bias near and exactly at the domain wall is defined by polarization dynamics, as shown schematically in the figure below. The switching dynamics of polarization is determined by the lattice barriers and pinning effects, which are not considered in the static LGD modeling.

To get insight into the mechanisms of the observed phenomena, we performed finite element modeling (FEM). Since the bending changes the shape of the CIPS layer, FEM results are presented in the local coordinate frame linked with the instant position of crystallographic axes inside the bent layer. The local normal axis  $x_n$  coincides with z, and the tangential axis  $x_t$  coincides with x for the flat layer (see Figure 5). Below all physical quantities (e.g., polarization components  $P_n$  and  $P_v$  electric field components,  $E_n$  and  $E_v$  and elastic strains components,  $u_{tv}$   $u_{tv}$  and  $u_{nn}$ ) are written in the local coordinate frame,  $\{x_n, x_v, z\}$ .

Distribution of the normal and tangential polarization components,  $P_n$  and  $P_b$  inside the flat 5 nm thick CIPS layer suspended between the patterns is shown in the top rows of Figure A2a,b, respectively. Since the top and bottom surfaces

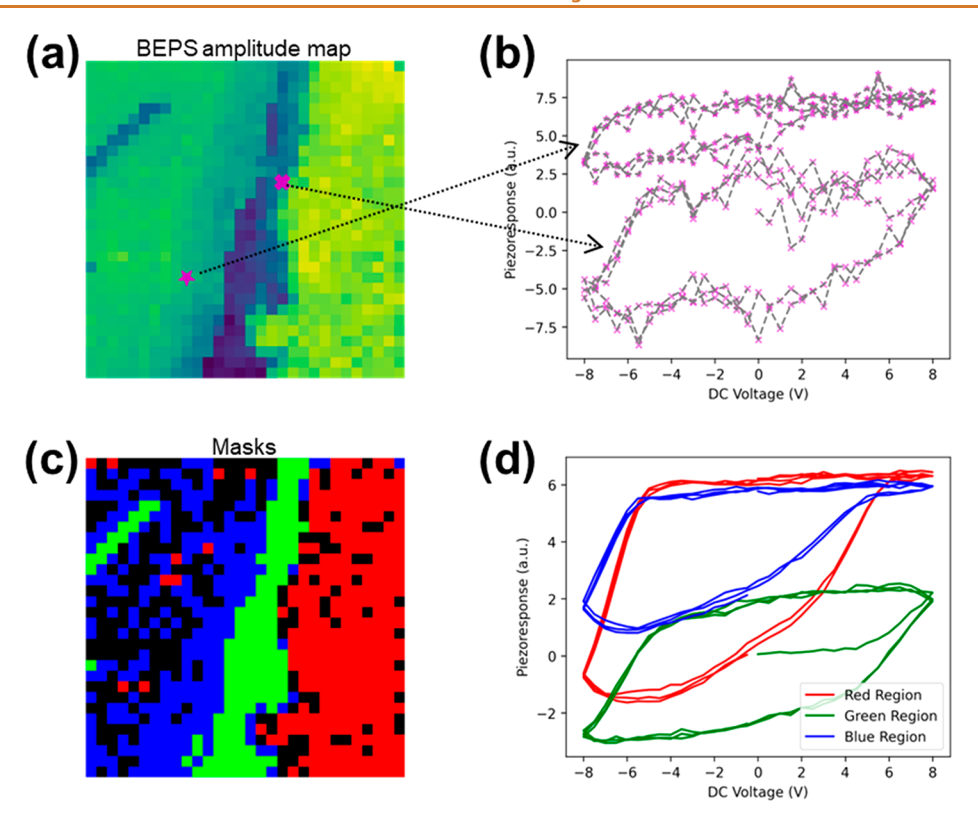


Figure 4. Band excitation piezoresponse spectroscopy (BEPS) results of the artificial bending domains. (a) Amplitude image showing the domain structure. (b) Two example BEPS spectra from the marked locations in (a). (c) Masks correspond to the different domain regions. (d), Averaged BEPS from the corresponding regions in (c).

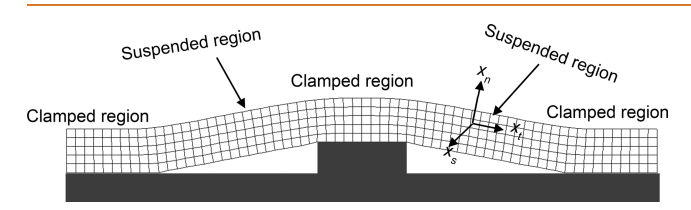


Figure 5. Typical mesh in the bent CIPS nanoflake on the patterned substrate, which is suspended between the patterns and clamped in the regions of the pattern "tops". The pattern lateral size is 50 nm, the height varies from 0 to 5 nm, and the period is 350 nm.

of the layer are regarded perfectly screened, the single-domain ferrielectric state with the polarization  $P_n \sim 3 \ \mu\text{C/cm}^2$ (abbreviated as "FI1") is stable in the flat or slightly bent layer. An isostructural transition from the FI1 state to the ferrielectric state with lower polarization  $P_n \sim 0.5 \ \mu\text{C/cm}^2$ (abbreviated as "FI2") occurs with the bending increase. The FI1-FI2 boundary is relatively sharp (~2.5 nm), because the interface between the FI1 and FI2 regions is almost unchanged. Due to the absence of the uncompensated bound charge, the depolarization electric field is absent inside the flat layer, and negligibly small at the flat FI1-FI2 boundary (see the top rows in Figure A3a,b, respectively). The piezoelectric response of the bent region is measured by PFM as shown in Figure 3, it is worth pointing out that the PFM signal is correlated to polarization but is not a quantitative measure of it. In most simple form, the relationship between polarization and piezoelectric properties is determined by the electrostrictive coupling, which expansion in the long-range ordered phase in the powers of spontaneous polarization gives the piezoelectric response. In PFM, the

contributions of the dielectric anisotropy, full piezoelectric tensor components, and elastic properties have been explored for 25 years until now.  $^{38-40}$ 

Correlations between the distributions of elastic strains components,  $u_{tt}$ ,  $u_{tn}$ , and  $u_{nn}$ , polarization components,  $P_n$  and  $P_t$ , and electric field components,  $E_n$  and  $E_t$ , in the suspended CIPS layer are shown in Figure 6 for different heights of patterning.

With an increase in the step height below the critical value, the layer bending increases, and well-localized features of polarization, field, and strains appear in the inflection points [see Figure 6a and Figures A2-A4]. When the pattern height (and so the bending) exceeds the critical value, the FI2 regions rapidly grow and fill in the inflection regions, where the layer is locally flat, as shown in Figure 6b, and Figures A2-A4. When the pattern height increases further, the FI2 regions expand and, simultaneously, the regions of FI1 states begin to shrink. Thus, the critical bending of the layer creates the inflected regions, where the FI2 states are stable and significantly increases the normal polarization component up to  $4 \mu \text{C/cm}^2$ in all layers except for the inflection regions with small  $P_n \sim 0.4$  $\mu$ C/cm<sup>2</sup>. The thin boundaries between the FI1 and FI2 states have a small and sign-alternating  $P_t$  (about 0.2  $\mu$ C/cm<sup>2</sup>), which reaches a maximum at the boundaries.

The FEM results, in addition to those shown in Figure 6, demonstrate that the domain walls appear in the regions of maximal stress and/or bending. In particular, they appear near the clamped tops boundaries ("up-bending" regions), as well as in the deep valleys ("down-bending" regions). The domain walls in the valleys are very sensitive even to the small external electric field, and electro-mobile, because any sort of pinning center is not considered in the LGD model. The domain walls

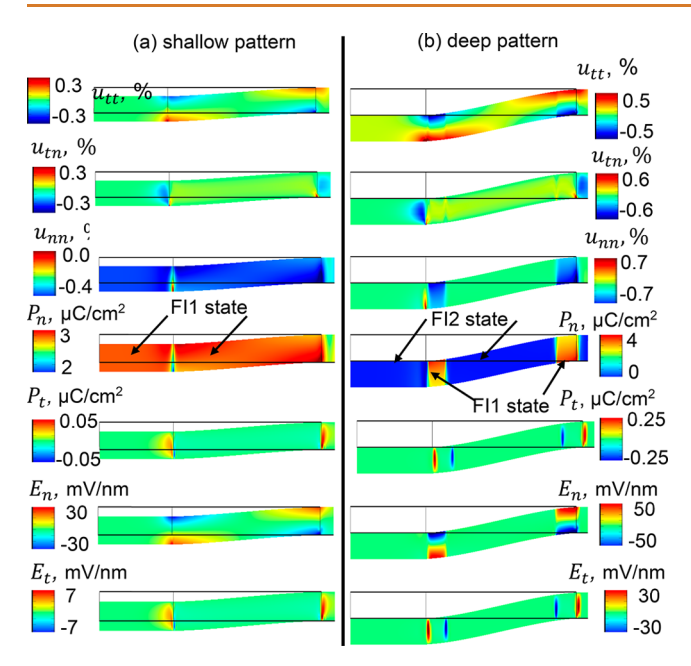


Figure 6. Correlations between the distributions of elastic strains components,  $u_{tv}$   $u_{tv}$ , and  $u_{nn}$ , polarization components,  $P_n$  and  $P_v$  and the field components,  $E_n$  and  $E_v$  in the suspended CIPS layer for different height of patterning, namely, 1.7 nm (a) and 5 nm (b). Thin black lines represent initial shape of the flat layer which has an actual shape of rectangle with the 5 nm height of and 155 nm wide. The top and bottom surfaces of the layer are perfectly screened; calculations are performed at 293 K. Color scales show the strain components in %, polarization components in  $\mu$ C/cm², and field components in mV/nm.

near the clamped tops are much less sensitive to the field because the clamping area acts as an expanded topological defect. Therefore, the high electric field caused by the PFM probe apex easily moves the domain walls toward the clamped tops, partially or completely destroying the down-bending domains.

To provide further insight, we develop the mesoscopic Landau—Ginsburg—Devonshire (LGD) theory for slightly bent CIPS layers. We consider different contributions to the static electric polarization of corrugated CIPS film, which is a semiconducting, flexoelectric, piezoelectric, and uniaxial ferrielectric low-dimensional material. Let us also assume that the bending is very small, and so  $P_n \approx P_3$  in the first approximation.

For a ferroelectric with the one-component out-of-plane spontaneous polarization  $P_3$ , the bulk density of the LGD functional F depends on  $P_3$ , elastic stress  $\sigma_b$  and their gradients and has the following form:  $^{27,41}$ 

$$F = \frac{\alpha}{2}P_{3}^{2} + \frac{\beta}{4}P_{3}^{4} + \frac{\gamma}{6}P_{3}^{6} + \frac{\delta}{8}P_{3}^{8} + \frac{g}{2}\left(\frac{\partial P_{3}}{\partial x_{i}}\right)^{2} - P_{i}E_{i}$$

$$- Q_{i3}\sigma_{i}P_{3}^{2} - Z_{i33}\sigma_{i}P_{3}^{4} - \frac{F_{ii3j}}{2}\left(P_{3}\frac{\partial \sigma_{i}}{\partial x_{j}} - \sigma_{i}\frac{\partial P_{3}}{\partial x_{j}}\right) - \frac{s_{ii}}{2}\sigma_{i}^{2}$$

$$- s_{ij}\sigma_{i}\sigma_{j}$$
(1)

According to Landau theory,<sup>42</sup> the coefficient  $\alpha$  linearly depends on the temperature T for proper ferroics,  $\alpha(T) = \alpha_T(T-T_{\rm C})$ , where  $T_{\rm C}$  is the Curie temperature. All other coefficients in eq 1 are supposed to be temperature independent. The coefficient  $\delta \geq 0$  is for the stability of the

free energy for all  $P_3$  values. The gradient coefficient g determines the magnitude of the gradient energy.  $E_i$  is the electric field. The values  $Q_{ijkl}$  and  $Z_{ijkl}$  are the linear and nonlinear electrostriction stress tensor components, respectively.  $F_{ijkl}$  is the flexoelectric stress tensor  $^{43}$  determined by the microscopic properties of the material. Einstein summation over repeated indexes is used hereinafter. The values  $T_{\rm C}$ ,  $\alpha_T$ ,  $\beta$ ,  $\gamma$  and  $\delta$ ,  $Q_{ijkl}$  and  $Z_{ijkl}$  given in Table AI in the Supporting Information, were defined in ref 26.

The electric field  $E_i$  is expressed via the potential  $\varphi$ , as  $E_i = -\frac{\partial \varphi}{\partial x_i}$ . The potential satisfies the Poisson equation, and we assume that  $|e\varphi| \ll k_{\rm B}T$  and introduce the Debye–Hukkel screening length,  $L_{\rm D} = \sqrt{\frac{k_{\rm B}T\varepsilon_0\varepsilon_{\rm b}}{2e^2n_0}}$ , where  $\varepsilon_0$  is a universal dielectric constant,  $\varepsilon_{\rm b}$  is the background dielectric constant,  $^{46}$  and  $n_0$  is the free carrier density in the unstrained material at  $\varphi$  = 0 (see in the Supporting Information for details).

Note that the surface corrugation can be expanded in Fourier series, whose each term can induce the dependence of the harmonic displacement of the CIPS layer along the X- or Y-axis. For the sake of simplicity, only one-component elastic field is considered, and only one component of the stress tensor,  $\sigma_3$ , is assumed to be nonzero and modulated in the direction x:

$$\sigma_3(x) = \sigma_3^m \cos(kx) \tag{2}$$

Here  $\sigma_3^m$  is the amplitude and  $\frac{2\pi}{k}$  is the stress period. Allowing for the Debye–Hukkel approximation, the variation of the free energy (1) yields

$$(\alpha - 2Q_{ij33}\sigma_{ij})P_3 + (\beta - 4Z_{ij33}\sigma_{ij})P_3^3 + \gamma P_3^5 + \delta P_3^7 - g\frac{\partial^2 P_3}{\partial x_i^2} = E_3 + F_{ii3j}\frac{\partial \sigma_i}{\partial x_j}$$
(3)

Under the condition  $k^2L_D^2 \ll 1$ , valid hereinafter due to the high electric conductivity of narrow-gap CIPS, the depolarization contribution can be small enough.

From eq 3, that the local change of Curie temperature can be derived as

$$T_{\rm LC}(\vec{x}) = T_{\rm C} + \frac{2}{\alpha_T} Q_{33} \sigma_3(x) - \frac{k^2}{\alpha_T \varepsilon_0 (\varepsilon_{\rm b} k^2 + L_{\rm D}^{-2})}$$
 (4)

However, the "local" expression has very little relation to the dependence of the phase transition temperature,  $T_{\rm pv}$  as a function of average curvature, which can be measured experimentally. The latter is a "global" coordinate-independent value, because the phase transition may occur in a spatial region much bigger than the period  $\frac{2\pi}{k}$  of a strain/corrugation. In this case,  $T_{\rm pt} \approx T_C$  because the average value  $\langle \sigma_3(\vec{x}) \rangle \approx 0$ . However, when the lateral size  $L \sim \frac{2\pi}{k}$  of a bent region becomes compatible or higher than the characteristic length of polarization correlations,  $L_c$ , the local phase transition may occur in the region.

Using the decoupling approximation,  $^{47,48}$  the vertical displacement  $U_i$  of CIPS surface, can be estimated under the PFM tip as  $^{38}$ 

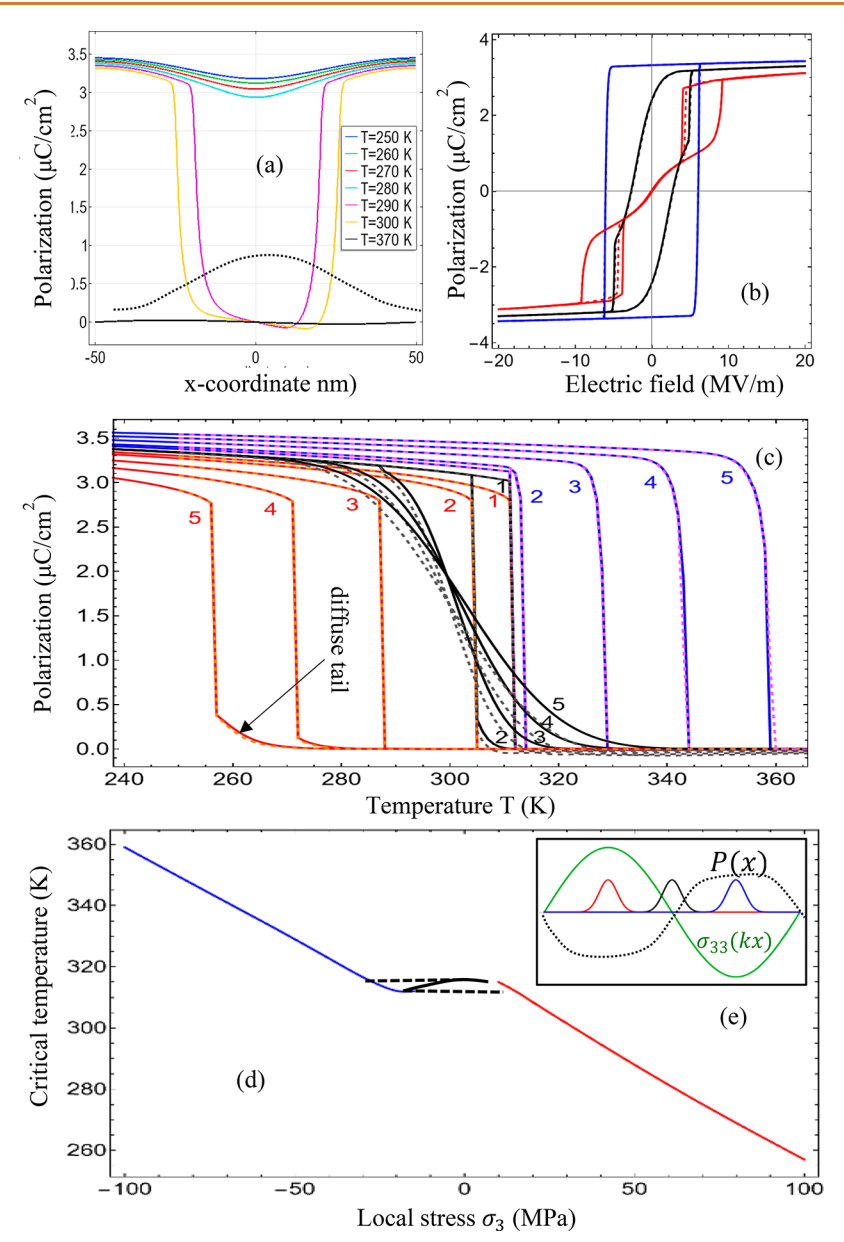


Figure 7. (a) Distribution of spontaneous polarization induced by a cosinusoidally modulated stress with the amplitude  $\sigma_3^m = 50$  MPa and period 100 nm calculated for several temperatures from 250 to 300 K (see legend for description of solid curves colors). Flexoelectric coefficient  $f = 2 \times 10^{-11}$  m<sup>3</sup>/C. The dotted curve is a schematical distribution of the stress distribution. (b) Quasi-static hysteresis loops of local polarization calculated at 298 K. Different loops correspond to the three 10 nm wide regions with maximal stress  $\sigma_3(x) = \sigma_3^m$  (red curves), zero stress  $\sigma_3(x) = 0$  (black curves), and minimal stress  $\sigma_3(x) = -\sigma_3^m$  (blue curves). (c) Temperature dependence of the spontaneous polarization values, which are averaged over three 10 nm wide regions, located near the points with maximal stress  $\sigma_3(x) = \sigma_3^m$  (red curves 1–5), zero stress  $\sigma_3(x) = 0$  (black curves 1–5), and minimal stress  $\sigma_3(x) = -\sigma_3^m$  (blue curves 1–5) with the amplitude  $\sigma_3^m = 15$ , 25, 50, 75, and 100 MPa (curves 1, 2, 3, 4 and 5, respectively). Flexoelectric coefficient f = 0 for solid curves and  $f = 2 \times 10^{-11}$  m<sup>3</sup>/C for dashed curves in the plots (b) and (c). (d) Stress dependence of the critical temperature, defined as the temperature values where the polarization sharply decreases (diffuse tails are neglected).

$$U_{l}(\vec{y}) \approx c_{kjmn} \int_{-\infty}^{\infty} d\xi_{1} \int_{-\infty}^{\infty} d\xi_{2} \int_{0}^{h} d\xi_{3} \frac{\partial G_{im}(-\xi_{1}, -\xi_{2}, \xi_{3})}{\partial \xi_{n}}$$

$$\times E_{l}(\vec{\xi}) d_{lkj}(\vec{y} - \vec{\xi})$$
(5)

where  $G_{im}(-\xi_1, -\xi_2, \xi_3)$  is a Green function and  $E_l(\vec{\xi})$  is an electric field induced by the PFM probe in the CIPS layer. The piezoelectric coefficients  $d_{lkj}(\vec{x})$  are proportional to the spontaneous polarization and dielectric susceptibility:<sup>49</sup>

$$d_{ijk}(\vec{x}) \approx 2\varepsilon_0 \chi \delta_{km} Q_{ijm3} P_3(\vec{x})$$
 (6)

where  $\chi$  is the linear dielectric susceptibility and  $\delta$  is a Kronecker-delta symbol. For the considered case of  $\sigma_3(x)$  given by eq 2, the dependence of  $\chi$  on k is analyzed in Figure B4 in the Supporting Information.

Expressions 5 and 6 imply that the surface displacement  $U_i$  is linearly proportional to the integral of  $P_3(\vec{x})$ , which variation is in turn proportional to the stress (or strain) and its gradient induced by the patterned substrate. For a flattened tip apex and small spontaneous polarization  $P_s$  (e.g., near the Curie temperature of CIPS, 293 K), a vertical PFM response, defined as  $d_{33}^{\text{eff}} = \frac{dU_3}{dV}$ , is proportional to the product  $\chi P_3(\vec{x})$ . In

a realistic case of a smooth corrugation and small  $L_{\rm D}$ , when  $kL_{\rm D}$   $\ll 1$ , we can use an estimation:

$$d_{33}^{\text{eff}} \sim Q_{33} \varepsilon_0 \chi \left( f_{3jkl} - \frac{\Sigma_{kl}^g}{2e} \right) \frac{\partial}{\partial x_j} u_{kl}(\vec{x}) + 2P_s (q_{lm33} + 2z_{lm33} P_s^2) u_{kl}(\vec{x})$$
(7)

Here  $f_{3jkl}$  is the flexoelectric strain tensor,  $q_{lm33}$  and  $z_{lm33}$  are the linear and nonlinear electrostriction strain tensor components, respectively, and  $\sum_{kl}^g$  is a deformation potential tensor. Expression 7 shows that the bending can create a smooth domain structure in a "weak" ferrielectric CIPS, and the structure determines the amplitude and phase of the PFM response.

Due to the strong, negative and temperature-dependent nonlinear electrostriction couplings  $(Z_{i33} < 0)$  and the "inverted" signs of the linear electrostriction coupling  $(Q_{33} < 0, Q_{23} > 0, \text{ and } Q_{13} > 0)$  for CIPS, the expected pressure effect on the local polarization switching is complex and unusual in comparison with many other ferroelectrics with  $Q_{33} > 0$ ,  $Q_{23} < 0$ , and  $Q_{13} < 0$ .

Results of numerical solution of eq 3 are shown in Figure 7 (see also Figures B1-B3 in the Supporting Information). From Figure 7a, the local stress changes the polarization profile; namely, it causes shallow wells, which exist in tensiled regions at temperatures 250–280 K, and deeper wells (up to P = 0), which exist in tensiled regions at temperatures 290-300 K. A relatively small increase (hills) of the polarization profile exists in compressed regions at temperatures 250-300 K. Figure 7b demonstrates the strong influence of periodic stress on the hysteresis loops shape, magnitude of the remanent polarization, and coercive fields (compare blue, black, and red loops). The rectangular-shaped loop at compressive stress, and double loops at tensile stress can be explained by the anomalous temperature dependence and "inverted" signs of CIPS linear and nonlinear electrostriction coupling coefficients. By varying the sign of applied stress (from expansion to compression) and its magnitude (from zero to several hundreds of MPa), a quasi-static double hysteresis loops can transform into pinched or single hysteresis loops (compare red, black, and blue loops).

The polarization hysteresis loops in Figure 7b are quite different from the experimental piezoresponse loops shown in Figure 4, because the modeling conditions are different from the experimental ones. The experimental loops correspond to the different distances from the domain wall: left far from the wall (red loop), right far from the wall (blue loop) and at the wall (green loop). Three loops in Figure 7b correspond to the three 10 nm wide regions with maximal stress  $\sigma_3(x) = \sigma_3^m$  (red curves), zero stress  $\sigma_3(x) = 0$  (black curves), and minimal stress  $\sigma_3(x) = -\sigma_3^m$  (blue curves). These loops are static loops, calculated without taking into consideration the polarization (and thus domain wall) dynamics, which is conditioned by the lattice barriers, pinning effects, and defects. As mentioned above, neither dynamic effects nor pinning effects are considered in the LGD modeling. Also, the local piezoresponse is not simply proportional to the polarization, because the influence of many factors, such as the PFM resolution function, the probe field penetration effects, and effective dielectric susceptibility, can make significant contribution to the loop shape. Figure B4 in the Supporting Information illustrates the transformations of the static loops in Figure 7b when the

simplest Landau—Khalatnikov dynamics is considered, and the bias window is smaller than the coercive bias for positive and zero stress (see solid curves in Figure B4). While the shape of solid loops is still far from the loops shown in Figure 4, they demonstrate the same trends, which allows us to conclude that the proposed LGD model is in qualitative agreement with PFM experiments.

From Figure 7c,d, the interaction of a ferrielectric soft mode with a periodic elastic deformation, induced by the patterned substrate, leads to the local shift of the phase transition temperature, and the temperature is higher for compressed regions [see the blue curves in Figure 7c and the blue line in Figure 7d], and lower for tensiled regions [see the blue curves in Figure 7c and the blue line in Figure 7d]. The local changes are visible only if the stress period is much longer than the correlation length. The change in the phase transition temperature, averaged over the corrugation period, is equal to zero. This is due to the fact that the average stress is zero. So, curved but stress-free regions look indifferent to the phase transition shift. Polarization averaging over the 10 nm wide region imitates the Gaussian field caused by a 10 nm size of the PFM tip-surface contact, and is schematically shown in Figure 7e. Polarization ripples, schematically shown by the black dotted curve in the inset, are caused by modulated stress, shown by the green curve.

The flexoelectric effect induces a relatively small built-in electric field on the right-hand side of eq 3, which induces a slight asymmetry of polarization profiles, as shown in Figure 7a, leads to a slight horizonal shift of local polarization hysteresis, as shown by dashed curves in Figure 7b, and smears the phase transition point, as shown by dashed curves in Figure 7c,d. The asymmetry and smearing become stronger with an increase in the stress amplitude [compare, e.g., Figures B1(c) and B1(d) in the Supporting Information]. As expected, the role of the flexoelectric effect becomes much stronger near the phase transition point.

#### **CONCLUSIONS**

To summarize, we explore the effect of bending on the ferroelectric domains in CIPS flakes. In the PFM experiment, we observed bending induced domains in the CIPS film and different polarization-voltage hysteresis loops in the bending regions and nonbinding regions. Our simulation results show that bending can create a smooth domain structure in a "weak" ferrielectric CIPS, and the structure determines the amplitude and phase of the PFM response. The local stress changes the polarization profile by causing shallow wells, which exist in tensile regions at temperatures 250-300 K. A relatively small increase (hills) of the polarization profile exists in compressed regions at the same temperatures. The periodic stress shows a strong influence on the shape of the hysteresis loops (consistent with experimental observation), magnitude of the remanent polarization, and coercive fields. The square-shaped loop at compressive stress and double loops at tensile stress can be explained by the anomalous temperature dependence and "inverted" signs of CIPS linear and nonlinear electrostriction coupling coefficients. The local changes are visible only if the stress period (e.g., alternative compressive and tensile stress at curved regions) is much higher than the correlation length; thus, a full measure of this change in PFM is challenging because PFM measures the net effect averaged over both compressive and tensile stress regions near the curvature. The change of the phase transition temperature,

averaged over the corrugation period, is equal to zero. This is due to the fact that the average stress is zero. So, curved, but stress-free, regions look indifferent to the phase transition shift. The flexoelectric effect induces a relatively small built-in electric field, which induces a slight asymmetry of polarization profiles, leads to a slight horizontal shift of local polarization hysteresis, and smears the phase transition point. The role of the flexoelectric effect becomes much stronger near the phase transition point.

#### **METHODS**

Piezoresponse force microscopy (PFM) measurements were performed on a commercial Cypher, Asylum Research and Oxford Instrument Company AFM system using a ElectriMulti75-G, a Budget Sensors tip with Pt/Ir coating, and a stiffness of ~3 N/m. BEPFM and BEPS were performed with a band of frequencies (bandwidth ~100 kHz) near the resonance frequency (~340 kHz).

### **ASSOCIATED CONTENT**

# **Supporting Information**

The Supporting Information is available free of charge at https://pubs.acs.org/doi/10.1021/acsnano.3c08603.

Appendix A, finite element modeling of ferroelectric CuInP<sub>2</sub>S<sub>6</sub> at stress (LGD parameters, mesh schematic, distribution of normal and tangential polarization components, field components, and shear strain components in bent CuInP<sub>2</sub>S<sub>6</sub>); Appendix B, Approximate analytical description (redistribution of spontaneous polarization induced by a cosinusoidally modulated stress, temperature dependence of spontaneous polarization values, quasi-static hysteresis loops of local polarization at difference stress, transformation of the loops when the simplest Landau—Khalatnikov dynamics is considered, temperature dependence of the effective dielectric susceptibility real part); Appendix C, bias window concept (illustration of bias window concept) (PDF)

# **AUTHOR INFORMATION**

## **Corresponding Authors**

Yongtao Liu — Center for Nanophase Materials Sciences, Oak Ridge National Laboratory, Oak Ridge, Tennessee 37830, United States; oorcid.org/0000-0003-0152-1783; Email: liuy3@ornl.gov

Sergei Kalinin — Department of Materials Science and Engineering, The University of Tennessee, Knoxville, Tennessee 37996, United States; Email: sergei2@utk.edu

### **Authors**

Anna N. Morozovska — Institute of Physics, National Academy of Sciences of Ukraine, 03028 Kyiv, Ukraine; orcid.org/0000-0002-8505-458X

Ayana Ghosh — Computational Sciences and Engineering Division, Oak Ridge National Laboratory, Oak Ridge, Tennessee 37830, United States; orcid.org/0000-0002-0432-3689

Kyle P. Kelley – Center for Nanophase Materials Sciences, Oak Ridge National Laboratory, Oak Ridge, Tennessee 37830, United States; Oorcid.org/0000-0002-7688-0484

Eugene A. Eliseev – Institute for Problems of Materials Science, National Academy of Sciences of Ukraine, 03142 Kyiv, Ukraine Jinyuan Yao — Department of Physics, Pennsylvania State University, University Park, Pennsylvania 16802, United States; orcid.org/0009-0006-0058-6605

Ying Liu – Department of Physics, Pennsylvania State University, University Park, Pennsylvania 16802, United States

Complete contact information is available at: https://pubs.acs.org/10.1021/acsnano.3c08603

# **Author Contributions**

Yongtao Liu and S.K. conceived the project. Yongtao Liu performed experiments and data analysis; A.N.M. and E.A.E. performed modeling; J.Y. and Ying Liu prepared samples. All authors contributed to discussions of results and manuscript.

#### Notes

The authors declare no competing financial interest.

#### **ACKNOWLEDGMENTS**

This effort (materials synthesis, PFM measurements) was supported as part of the center for 3D Ferroelectric Microelectronics (3DFeM), an Energy Frontier Research Center funded by the U.S. Department of Energy (DOE), Office of Science, Basic Energy Sciences under Award Number DE-SC0021118. The research (PFM measurements) was performed and partially supported at Oak Ridge National Laboratory's Center for Nanophase Materials Sciences (CNMS), a U.S. Department of Energy, Office of Science User Facility, under user proposal CNMS2023-A-01858. The growth of single crystals of CIPS used in this work was supported by the National Science Foundation through the Penn State 2D Crystal Consortium-Materials Innovation Platform (2DCC-MIP) under NSF cooperative agreement DMR-1539916, and DMR-2039351. A.N.M. acknowledges support from the National Research Fund of Ukraine (project "Low-dimensional graphene-like transition metal dichalcogenides with controllable polar and electronic properties for advanced nanoelectronics and biomedical applications", grant application 2020.02/0027). E.A.E. acknowledges support from the National Academy of Sciences of Ukraine.

## **REFERENCES**

- (1) Novoselov, K. S.; Geim, A. K.; Morozov, S. V.; Jiang, D.-e.; Zhang, Y.; Dubonos, S. V.; Grigorieva, I. V.; Firsov, A. A. Electric field effect in atomically thin carbon films. *science* **2004**, *306* (5696), 666–660
- (2) Manzeli, S.; Ovchinnikov, D.; Pasquier, D.; Yazyev, O. V.; Kis, A. 2D transition metal dichalcogenides. *Nature Reviews Materials* **2017**, 2 (8), 17033.
- (3) Mayorov, A. S.; Gorbachev, R. V.; Morozov, S. V.; Britnell, L.; Jalil, R.; Ponomarenko, L. A.; Blake, P.; Novoselov, K. S.; Watanabe, K.; Taniguchi, T. Micrometer-scale ballistic transport in encapsulated graphene at room temperature. *Nano Lett.* **2011**, *11* (6), 2396–2399.
- (4) Balandin, A. A. Thermal properties of graphene and nano-structured carbon materials. *Nature materials* **2011**, *10* (8), 569–581.
- (5) Yankowitz, M.; Chen, S.; Polshyn, H.; Zhang, Y.; Watanabe, K.; Taniguchi, T.; Graf, D.; Young, A. F.; Dean, C. R. Tuning superconductivity in twisted bilayer graphene. *Science* **2019**, *363* (6431), 1059–1064.
- (6) Wang, L.; Shih, E.-M.; Ghiotto, A.; Xian, L.; Rhodes, D. A.; Tan, C.; Claassen, M.; Kennes, D. M.; Bai, Y.; Kim, B. Correlated electronic phases in twisted bilayer transition metal dichalcogenides. *Nature materials* **2020**, *19* (8), 861–866.
- (7) Kerelsky, A.; McGilly, L. J.; Kennes, D. M.; Xian, L.; Yankowitz, M.; Chen, S.; Watanabe, K.; Taniguchi, T.; Hone, J.; Dean, C.

- Maximized electron interactions at the magic angle in twisted bilayer graphene. *Nature* **2019**, *572* (7767), 95–100.
- (8) Choi, Y.; Kemmer, J.; Peng, Y.; Thomson, A.; Arora, H.; Polski, R.; Zhang, Y.; Ren, H.; Alicea, J.; Refael, G. Electronic correlations in twisted bilayer graphene near the magic angle. *Nat. Phys.* **2019**, *15* (11), 1174–1180.
- (9) Huang, B.; Clark, G.; Navarro-Moratalla, E.; Klein, D. R.; Cheng, R.; Seyler, K. L.; Zhong, D.; Schmidgall, E.; McGuire, M. A.; Cobden, D. H. Layer-dependent ferromagnetism in a van der Waals crystal down to the monolayer limit. *Nature* **2017**, *546* (7657), 270–273.
- (10) Belianinov, A.; He, Q.; Dziaugys, A.; Maksymovych, P.; Eliseev, E.; Borisevich, A.; Morozovska, A.; Banys, J.; Vysochanskii, Y.; Kalinin, S. V. CuInP2S6 room temperature layered ferroelectric. *Nano Lett.* **2015**, *15* (6), 3808–3814.
- (11) Kalinin, S. V.; Meunier, V. Electronic flexoelectricity in low-dimensional systems. *Phys. Rev. B* **2008**, 77 (3), No. 033403.
- (12) Dai, Z.; Liu, L.; Zhang, Z. Strain engineering of 2D materials: issues and opportunities at the interface. *Adv. Mater.* **2019**, *31* (45), No. 1805417.
- (13) Zhang, Y.; Heiranian, M.; Janicek, B.; Budrikis, Z.; Zapperi, S.; Huang, P. Y.; Johnson, H. T.; Aluru, N. R.; Lyding, J. W.; Mason, N. Strain modulation of graphene by nanoscale substrate curvatures: a molecular view. *Nano Lett.* **2018**, *18* (3), 2098–2104.
- (14) Yang, W.; Chen, S.; Ding, X.; Sun, J.; Deng, J. Reducing Threshold of Ferroelectric Domain Switching in Ultrathin Two-Dimensional CuInP2S6 Ferroelectrics via Electrical—Mechanical Coupling. J. Phys. Chem. Lett. 2023, 14, 379—386.
- (15) Sun, Z.-Z.; Xun, W.; Jiang, L.; Zhong, J.-L.; Wu, Y.-Z. Strain engineering to facilitate the occurrence of 2D ferroelectricity in CuInP2S6 monolayer. *J. Phys. D: Appl. Phys.* **2019**, 52 (46), No. 465302.
- (16) Chen, C.; Liu, H.; Lai, Q.; Mao, X.; Fu, J.; Fu, Z.; Zeng, H. Large-scale domain engineering in two-dimensional ferroelectric CuInP2S6 via giant flexoelectric effect. *Nano Lett.* **2022**, 22 (8), 3275–3282.
- (17) Rahman, S.; Yildirim, T.; Tebyetekerwa, M.; Khan, A. R.; Lu, Y. Extraordinary Nonlinear Optical Interaction from Strained Nanostructures in van der Waals CuInP2S6. ACS Nano 2022, 16 (9), 13959–13968.
- (18) Ming, W.; Huang, B.; Zheng, S.; Bai, Y.; Wang, J.; Wang, J.; Li, J. Flexoelectric engineering of van der Waals ferroelectric CuInP2S6. *Science Advances* **2022**, *8* (33), No. eabq1232.
- (19) Liu, F.; You, L.; Seyler, K. L.; Li, X.; Yu, P.; Lin, J.; Wang, X.; Zhou, J.; Wang, H.; He, H. Room-temperature ferroelectricity in CuInP2S6 ultrathin flakes. *Nat. Commun.* **2016**, *7* (1), 12357.
- (20) Brehm, J. A.; Neumayer, S. M.; Tao, L.; O'Hara, A.; Chyasnavichus, M.; Susner, M. A.; McGuire, M. A.; Kalinin, S. V.; Jesse, S.; Ganesh, P. Tunable quadruple-well ferroelectric van der Waals crystals. *Nat. Mater.* **2020**, *19* (1), 43–48.
- (21) Morozovska, A. N.; Eliseev, E. A.; Kelley, K.; Kalinin, S. V. Temperature-Assisted Piezoresponse Force Microscopy: Probing Local Temperature-Induced Phase Transitions in Ferroics. *Physical Review Applied* **2022**, *18* (2), No. 024045.
- (22) Osada, M.; Sasaki, T. The rise of 2D dielectrics/ferroelectrics. *APL Materials* **2019**, 7 (12), No. 120902.
- (23) Wu, M.; Jena, P. The rise of two-dimensional van der Waals ferroelectrics. Wiley Interdisciplinary Reviews: Computational Molecular Science 2018, 8 (5), No. e1365.
- (24) Susner, M. A.; Chyasnavichyus, M.; Puretzky, A. A.; He, Q.; Conner, B. S.; Ren, Y.; Cullen, D. A.; Ganesh, P.; Shin, D.; Demir, H. Cation—eutectic transition via sublattice melting in CuInP2S6/In4/3P2S6 van der Waals layered crystals. *ACS Nano* **2017**, *11* (7), 7060—7073
- (25) Tolédano, P.; Guennou, M. Theory of antiferroelectric phase transitions. *Phys. Rev. B* **2016**, *94* (1), No. 014107.
- (26) Morozovska, A. N.; Eliseev, E. A.; Kalinin, S. V.; Vysochanskii, Y. M.; Maksymovych, P. Stress-induced phase transitions in nanoscale Cu In P 2 S 6. *Phys. Rev. B* **2021**, *104* (5), No. 054102.

- (27) Bourdon, X.; Maisonneuve, V.; Cajipe, V.; Payen, C.; Fischer, J. Copper sublattice ordering in layered CuMP2Se6 (M= In, Cr). *Journal of alloys and compounds* **1999**, 283 (1–2), 122–127.
- (28) Susner, M. A.; Chyasnavichyus, M.; McGuire, M. A.; Ganesh, P.; Maksymovych, P. Metal thio-and selenophosphates as multifunctional van der Waals layered materials. *Adv. Mater.* **2017**, 29 (38), No. 1602852.
- (29) Maisonneuve, V.; Cajipe, V.; Simon, A.; Von Der Muhll, R.; Ravez, J. Ferrielectric ordering in lamellar CuInP2S6. *Phys. Rev. B* **1997**, *56* (17), 10860.
- (30) Banys, J.; Dziaugys, A.; Glukhov, K. E.; Morozovska, A. N.; Morozovsky, N. V.; Vysochanskii, Y. M. Van Der Waals Ferroelectrics: Properties and Device Applications of Phosphorous Chalcogenides; John Wiley & Sons, 2022.
- (31) Niu, L.; Liu, F.; Zeng, Q.; Zhu, X.; Wang, Y.; Yu, P.; Shi, J.; Lin, J.; Zhou, J.; Fu, Q. Controlled synthesis and room-temperature pyroelectricity of CuInP2S6 ultrathin flakes. *Nano Energy* **2019**, *58*, 596–603.
- (32) Yao, J.; Liu, Y.; Ding, S.; Zhu, Y.; Mao, Z.; Kalinin, S. V.; Liu, Y. Ferroelectric Schottky diodes of CuInP2S6 nanosheet. *Appl. Phys. Lett.* **2023**, *123* (14), 142903.
- (33) Wang, K.; Li, D.; Wang, J.; Hao, Y.; Anderson, H.; Yang, L.; Hong, X. Interface-tuning of ferroelectricity and quadruple-well state in CuInP2S6 via ferroelectric oxide. ACS Nano 2023, 17, 15787.
- (34) Xu, D.-D.; Ma, R.-R.; Fu, A.-P.; Guan, Z.; Zhong, N.; Peng, H.; Xiang, P.-H.; Duan, C.-G. Ion adsorption-induced reversible polarization switching of a van der Waals layered ferroelectric. *Nat. Commun.* **2021**, *12* (1), 655.
- (35) Balke, N.; Neumayer, S. M.; Brehm, J. A.; Susner, M. A.; Rodriguez, B. J.; Jesse, S.; Kalinin, S. V.; Pantelides, S. T.; McGuire, M. A.; Maksymovych, P. Locally controlled Cu-ion transport in layered ferroelectric CuInP2S6. ACS Appl. Mater. Interfaces 2018, 10 (32), 27188–27194.
- (36) Zhou, S.; You, L.; Chaturvedi, A.; Morris, S. A.; Herrin, J. S.; Zhang, N.; Abdelsamie, A.; Hu, Y.; Chen, J.; Zhou, Y. Anomalous polarization switching and permanent retention in a ferroelectric ionic conductor. *Materials Horizons* **2020**, *7* (1), 263–274.
- (37) Aravind, V. R.; Morozovska, A. N.; Bhattacharyya, S.; Lee, D.; Jesse, S.; Grinberg, I.; Li, Y.; Choudhury, S.; Wu, P.; Seal, K. Correlated polarization switching in the proximity of a 180 domain wall. *Phys. Rev. B* **2010**, 82 (2), No. 024111.
- (38) Morozovska, A. N.; Eliseev, E. A.; Bravina, S. L.; Kalinin, S. V. Resolution-function theory in piezoresponse force microscopy: Wall imaging, spectroscopy, and lateral resolution. *Phys. Rev. B* **2007**, *75* (17), No. 174109.
- (39) Morozovska, A. N.; Eliseev, E. A.; Kalinin, S. V. The piezoresponse force microscopy of surface layers and thin films: Effective response and resolution function. *J. Appl. Phys.* **2007**, *102* (7), 074105.
- (40) Eliseev, E. A.; Morozovska, A. N.; Ievlev, A. V.; Balke, N.; Maksymovych, P.; Tselev, A.; Kalinin, S. V. Electrostrictive and electrostatic responses in contact mode voltage modulated scanning probe microscopies. *Appl. Phys. Lett.* **2014**, *104* (23), 232901.
- (41) Morozovska, A. N.; Eliseev, E. A.; Vysochanskii, Y. M.; Khist, V. V.; Evans, D. R. Screening-induced phase transitions in core-shell ferroic nanoparticles. *Physical Review Materials* **2022**, *6* (12), No. 124411.
- (42) Landau, L. D.; Lifšic, E. M.; Lifshitz, E. M.; Kosevich, A. M.; Pitaevskii, L. P. *Theory of elasticity*; Elsevier, 1986; Vol. 7.
- (43) Yudin, P.; Tagantsev, A. Fundamentals of flexoelectricity in solids. *Nanotechnology* **2013**, 24 (43), No. 432001.
- (44) Mashkevich, V. Electrical, optic and elastic properties of diamond-type crystals. *Sov. Phys.-JETP* **1957**, 5 (4), 707–713.
- (45) Kogan, S. M. Piezoelectric effect during inhomogeneous deformation and acoustic scattering of carriers in crystals. *Soviet Physics-Solid State* **1964**, *5* (10), 2069–2070.
- (46) Tagantsev, A. K.; Cross, L. E.; Fousek, J. Domains in ferroic crystals and thin films; Springer, 2010; Vol. 13.

- (47) Felten, F.; Schneider, G.; Saldaña, J. M.; Kalinin, S. Modeling and measurement of surface displacements in BaTiO 3 bulk material in piezoresponse force microscopy. *J. Appl. Phys.* **2004**, *96* (1), 563–568.
- (48) Scrymgeour, D. A.; Gopalan, V. Nanoscale piezoelectric response across a single antiparallel ferroelectric domain wall. *Phys. Rev. B* **2005**, 72 (2), No. 024103.
- (49) Smolensky, G. In Ferroelectrics and Related Materials; Smolensky, G., Eds.; Gordon and Breach Science Publishers: New York, 1984.